Concentration and Coverage Dependent Adlayer Structures: From Two-Dimensional Networks to Rotation in a Bearing

Christoph Meier,[||,†] Michael Roos,[‡] Daniela Künzel,[§] Achim Breitruck,[‡] Harry E. Hoster,[‡] Katharina Landfester,[†] Axel Gross,[§] R. Jürgen Behm,[‡] and Ulrich Ziener*[,†]

Institute of Organic Chemistry III Macromolecular Chemistry, Institute of Surface Chemistry and Catalysis, and Institute for Theoretical Chemistry, University of Ulm Albert-Einstein-Allee 11, D-89081 Ulm, Germany

Received: October 20, 2009

A bisterpyridine based molecule, **3,3′-BTP**, shows a variety of adlayer structures at the interface between highly oriented pyrolytic graphite (HOPG) and the liquid depending on the concentration in solution. Three closely related linear and one hexagonal 2D patterns are found. Comparison with the self-assembly at the HOPG|gas interface shows that in the absence of the solvent one of the linear and the hexagonal structures can be found. The concentration dependent order of appearance of the different surface structures is rationalized by a thermodynamic model. In the adlayer unit cell, the hexagonal phase offers a central void which is mostly filled with a seventh **3,3′-BTP** molecule. In the presence of the solvent, those molecules are presumably rotating, whereas at the HOPG|gas interface no clear rotation can be observed.

Introduction

There is a vast variety of literature on self-assembling monolayers (SAMs) at both the solid|liquid and the solid|gas interface. It is of utmost interest to get insight and understanding and finally control over the formation of those assemblies. In many cases molecular building blocks are tailored and thus programmed via functional groups with directed intermolecular interactions such as hydrogen bonding followed by a read-out of the information in the subsequent self-assembly process. Besides the intrinsic structural control, self-assembly behavior can be controlled by the variation of external parameters. At the solid|gas interface, i.e., under ultra high vacuum (UHV) conditions, surface coverage[1−5] and temperature[6] are external triggers which have substantial impact on the formation of SAMs. Deposition of molecular building blocks at the solid|liquid interface restricts the possible temperature range as a controlling parameter because of the melting point and the vapor pressure of the solution.[7] On the contrary, the solvent adds further variability to the system based on the solvent's nature and quality. In the literature, several examples for solvent dependent adlayer structures are found.[8−17] In most cases, the coadsorption of solvent molecules plays an important role in the stabilization of the molecular monolayers[18−21] but can also determine certain conformations of the solute molecules which are then assembled at the interface.[22]

In addition, the solution gives the opportunity to vary the concentration of the molecules in the supernatant at the solid|liquid interface. To the best of our knowledge, there are only very few systematic investigations on the solute concentration dependent two-dimensional (2D) self-assembly process.[23] Recently, concentration dependent 2D structures were described for alkoxylated annulenes.[23] Here, an interplay between weak alkyl−alkyl interactions and adlayer−substrate interactions stabilizes different adlayer phases. In the case of a binary supramolecular network, reversible phase transitions between six different adlayer phases could be induced by varying the ratio of both species and their dilution in the solution.[24] A monodendron isophthalic acid derivative undergoes a phase transition from lamella to hexamer with concentration decrease because of solvent coadsorption.[25,26] Although the self-assembly of organic molecules at the solid|liquid interface has been studied since the 1980s,[27] a comprehensive understanding of the formation of those assemblies is still in its infancy. The precise control over the morphology of the predominantly formed nanostructures on surfaces is of exceptional interest, as the physical and chemical properties of molecular monolayers is supposed to be directly linked to their structure.[28]

SCHEME 1: Schematic Representation of the Investigated Oligopyridine 3,3′-BTP

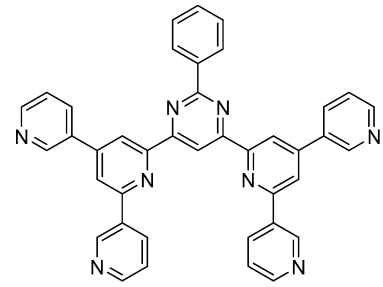

3,3'-BTP

The class of the C_{2v} symmetric oligopyridines shows a broad variety of self-assembling properties.[29,30] The interactions in 2D monolayers of those compounds are mainly governed by weak intermolecular hydrogen bonds leading to hydrogen bonded networks (HBN).[9] As recently reported, deposition of the oligopyridine **3,3′-BTP** (Scheme 1) onto highly oriented pyrolytic graphite (HOPG) from a high concentration solution leads to two densely packed linear structures without functional (host−guest) properties.[9] Deposition from a diluted solution though leads to the formation of additional adlayer structures.[29] The hexagonal quasi-porous structure preferentially formed from diluted solutions shows functional host−guest properties, dem-

† Institute of Organic Chemistry III Macromolecular Chemistry.
‡ Institute of Surface Chemistry and Catalysis.
§ Institute for Theoretical Chemistry.
|| Present address: Nanoscience Centre, University of Cambridge, 11 JJ Thomson Avenue, Cambridge CB3 0FF, United Kingdom.

10.1021/jp910029z

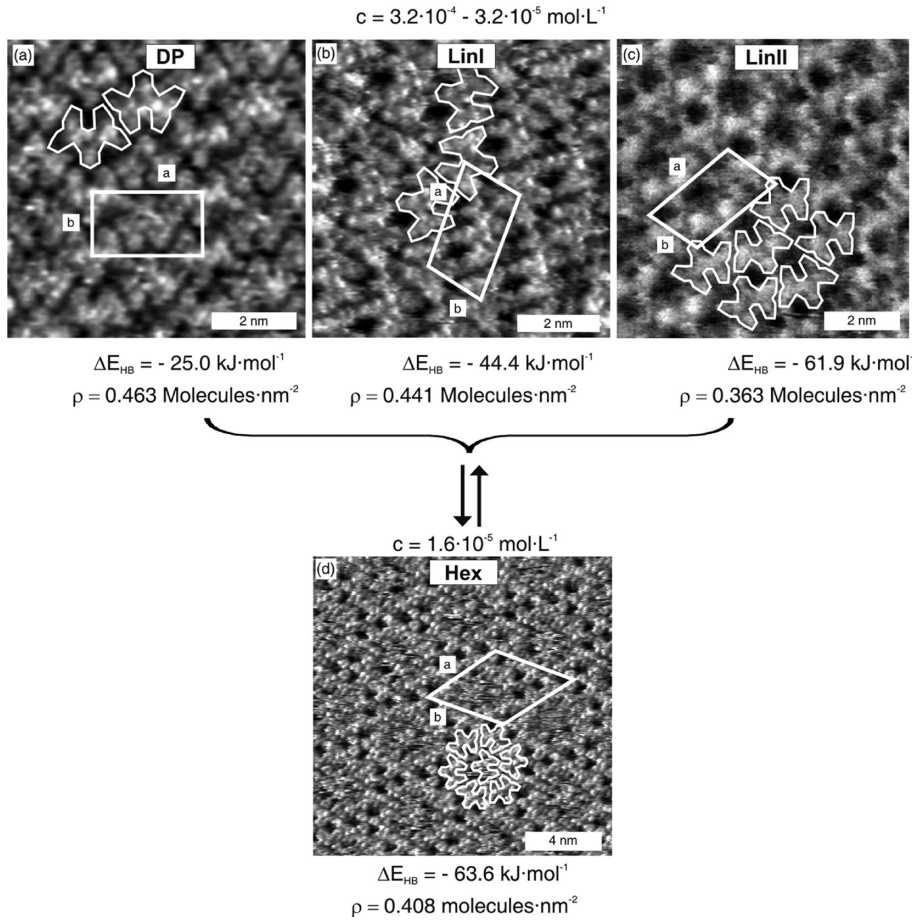

Figure 1. STM images of the observed coexistent adlayers at the solid|liquid interface: (a) the densely packed linear structure **DP**, (b) the linear derivative **LinI**, (c) the linear derivative **LinII**, and (d) the hexagonal structure **Hex**. The concentration of the oligopridines affects which stucture predominantly forms.

onstrating the ability to externally adjust the properties of molecular monolayers.

Here, we show that the ratio of the different coexistent 2D structures at the solid|liquid interface is closely associated with the concentration of the oligopyridine molecules in the supernatant solution, supporting in principle the thermodynamic model by Lei et al.;[23] but as a result of different and more complex intermolecular interactions for each type of adlayer, the system cannot be described with the recently published model.[23] In the present publication, results from complementary UHV studies and calculations were combined with the results from the solid|liquid interface to gain deeper insight into the formation of oligopyridine monolayers and to demonstrate a more general model for the prediction of concentration dependent adlayer structures at the solid|liquid interface by isothermal adsorption.

Experimental Section

The synthesis of the oligopyridine derivative **3,3′-BTP** was described previously.[9] 1,2,4-Trichlorobenzene (TCB) was used as received from commercial sources.

The scanning tunneling microscopy (STM) experiments at the solid|liquid interface were performed at ambient conditions with a commercially available low-current RHK SPM1000 STM with a resolution of 1024 × 1024 data points per image and a scan speed of 0.6 $\mu m \cdot s^{-1}$. Generally, after cleaving the highly ordered pyrolytic graphite (HOPG) surface with adhesive tape, the quality of the mechanically cut Pt|Ir(80|20) tip was tested through atomic resolution of the graphite surface. The atomically resolved graphite images were used for calibration of the distances and angles. After stopping the scanning process, a drop (10 μL) of a solution of **3,3′-BTP** in TCB was applied to the surface with the tip in tunnel contact. The tunneling current set point was between 10 to 20 pA and the bias voltage between −0.5 to −1.0 V. The STM images have not been subject to image processing except slope subtraction.

STM measurements at the solid|gas interface were carried out in a standard ultrahigh vacuum (UHV) chamber. For sample preparation, the chamber was equipped with a sample heater and an evaporator for the deposition of the **3,3′-BTP** molecules. All images at the solid|gas interface were recorded with a home-built STM in combination with a commercial I−V converter (10^{-9} V•A^{-1}, type IVP, RHK) and were acquired with tunnel currents of 2−100 pA and sample bias between −0.1 and −3.3 V. All images were recorded in the constant current mode. Highly oriented pyrolytic graphite (HOPG) (SPI-grade 3, SPI) substrates were prepared by tape stripping in air. For UHV measurements, the freshly cleaved HOPG substrate was transferred into the UHV system via a load−lock system and subsequently annealed at 1000 K for a prolonged time. Deposition of the **3,3′-BTP** molecules was performed by evaporation via a home-built, resistively heated Knudsen Cell (deposition rate, 0.1 molecules nm^{-2} min^{-1}; cell temperature, 583 K). The molecular networks were prepared by depositing 0.4 molecules•nm^{-2} on the surface. In an alternative approach for the preparation of these structures, the deposition time was

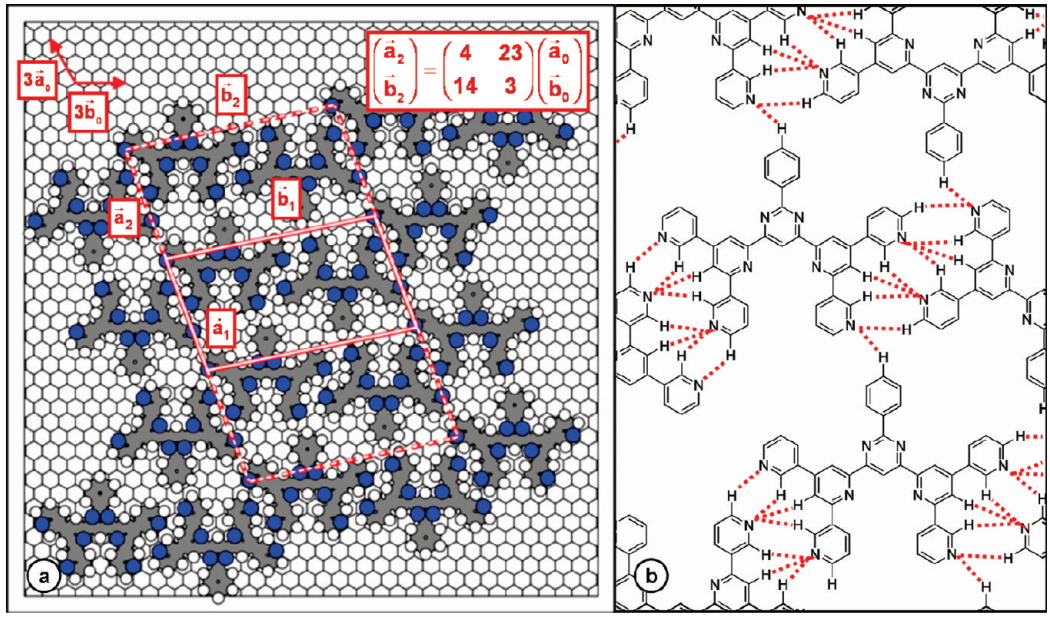

Figure 2. (a) Adsorption model of **LinII** with a molecular unit cell (solid) and a commensurate unit cell (dotted). (b) The asymmetric hydrogen bonding pattern of **LinII**.

increased, and the excess molecules were removed from the surface by heating to 551 or 546 K. Such elevated temperatures cause a desorption process and allow for a precise adjustment of the surface coverage, for instance, 0.4 molecules·nm^{-2} for the hexagonal structure.

Results and Discussion

Solid|Liquid Interface. ***Deposition from Concentrated Solution.*** As reported earlier, deposition of **3,3′-BTP** from a concentrated 1,2,4-trichlorobenzene (TCB) solution ($3.2\cdot10^{-4}$ mol·L^{-1}) leads to two linear 2D assemblies, the densely packed adlayer **DP** and its derivative **LinI** (Figure 1a and b).[9] In both structures, the oligopyridine molecules are arranged in a linear fashion, rotated 180° toward each other. The unit cell parameters were determinded to be $a_1 = 2.7 \pm 0.2$ nm, $b_1 = 1.6 \pm 0.2$ nm, and $\angle_{a,b} = 90 \pm 1°$ for **DP**, and $a_1 = 2.9 \pm 0.2$ nm, $b_1 = 1.6 \pm 0.2$ nm, and $\angle_{a,b} = 78 \pm 1°$ for **LinI**.[9] The packing density was calculated to 0.463 molecules·nm^{-2} for the **DP** phase and 0.441 molecules·nm^{-2} for the **LinI** phase. In the **DP** structure, the intermolecular interaction perpendicular to the molecular C_2 axis is symmetric, whereas in **LinI**, this interaction is asymmetric, resulting in homochiral enantiomorphic domains. For both structures **DP** and **LinI**, there was no preferential orientation to the substrate.

Deposition from Diluted Solutions. *Linear Structure.* At lower concentrations ($1.6\cdot10^{-5}$ mol·L^{-1}–$3.2\cdot10^{-5}$ mol·L^{-1}), the graphite surface is mainly covered with a linear structure **LinII** and a hexagonal network **Hex** (Figure 1c and d). The linear pattern **LinII** is of a structure similar to that of **LinI**, but with a slightly larger unit cell, which can be attributed to optimized intermolecular interactions (see below and Figure 2b). The molecules are also rotated 180° toward each other and lie side by side. The unit cell parameters were determined to be $a_1 = 1.77 \pm 0.04$ nm and $b_1 = 3.15 \pm 0.05$ nm, with an enclosing angle of $81 \pm 2°$. With two oligopyridine molecules per unit cell, the packing density amounts to 0.363 molecules·nm^{-2}. Subsequent STM images, comparing the adlayer orientation with that of the underlying substrate, revealed an angle between the C_2 molecular axis and a primitive substrate vector of $90 \pm 3°$. This indicates that in the adlayer **LinII** the adsorbate adopts a orientation coincident with the substrate (Figure 2a). DFT calculations reveal that the experimentally found orientation of the adsorbed oligopyridines in this structure on HOPG is the energetically most stable adsorption configuration (Supporting Information, Figure S8). In the case of phenylene-extended oligopyridine derivatives, only this adsorption configuration was found.[31]

The commensurate unit cell is three times bigger than the molecular unit cell and can be expressed in matrix notation as follows:

$$\begin{pmatrix}\vec{a}_2\\ \vec{b}_2\end{pmatrix} = \begin{pmatrix}4 & 23\\ 14 & 3\end{pmatrix}\begin{pmatrix}\vec{a}_0\\ \vec{b}_0\end{pmatrix}$$

with the substrate lattice vectors $\vec{a}_0$ and $\vec{b}_0$. The length of the adlayer lattice vectors in the adsorption model of $a_1 = 1.74$ nm, $b_1 = 3.15$ nm, and the enclosed angle of 81° are in good agreement with the experimental results and further support the proposed commensurate structure model.

Hexagonal Structure. The structure of the hexagonal pattern **Hex** is completely different from the structure of the linear networks. In **Hex**, the physisorbed oligopyridine molecules are rotated 60° toward each other, lying side by side (Figure 1d and Figure 3). Six molecules form a gearwheel-like molecular arrangement, exhibiting a cavity with a diameter of approximately 1.6 nm. This cavity was recently used to accommodate copper phthalocyanine.[29] The parameters of the C_s-symmetric unit cell were determined to be $a_1 = b_1 = 4.43 \pm 0.02$ nm, with an angle of $61 \pm 4°$. The unit cell vectors are rotated $13 \pm 1°$ versus the primitive vectors of the substrate (Figure 3), and the molecular C_2 axis encloses an angle of $85 \pm 1°$ with a primitive substrate vector. The structure characteristics derived from the STM images are consistent with the structure characteristics of the commensurate molecular model of the structure **Hex**. In matrix notation, the hexagonal unit cell can be expressed as follows:

$$\begin{pmatrix}\vec{a}_1\\ \vec{b}_1\end{pmatrix} = \begin{pmatrix}20 & 5\\ -5 & 15\end{pmatrix}\begin{pmatrix}\vec{a}_0\\ \vec{b}_0\end{pmatrix}$$

with the substrate lattice vectors $\vec{a}_0$ and $\vec{b}_0$. The length of the vectors is $a_1 = b_1 = 4.43$ nm, which agrees with the experimental results.

As already reported, additional oligopyridine molecules are coadsorbed in the cavities.[29] We experimentally determined the stabilization energy of the coadsorbed oligopyridine and described its exchange with a copper phthalocyanine molecule.[29] In this particular case, coadsorption of 1,2,4-trichlorobenzene solvent molecules is thermodynamically disfavored compared to the coadsorption of oligopyridine molecules. However, in porous monolayers built up from molecules which are too large to adsorb into the cavities, the coadsorption of small TCB molecules can be observed.[32] With the coadsorption of **3,3′-BTP** in the hexagonal cavities, the unit cell contains seven oligopyridine molecules, resulting in a packing density of 0.408 molecules·nm^{-2}. Without oligopyridine coadsorption, the packing density for a unit cell containing six oligopyridine molecules decreases to 0.350 molecules·nm^{-2}. In both systems reported earlier, a decrease in surface coverage correlates with the decrease in concentration.[23,24] However, the additional adsorption of building block molecules into cavities of the low concentration phase has not been reported. On the contrary, trimesic acid, for example, forms 2D porous hexagonal networks[14,33,34] which are able to incorporate various guest molecules[35−38] and even itself.[39]

In addition to the large cavities in the inner part of a hexagon, small diameter pores between neighboring hexagons are also visible. Since the phenyl rings of the molecules are pointing outward, two molecules with an including angle of 120° of adjacent hexagons enclose and, therefore, share two tiny pores. This results in six pores per unit cell indicated by green ellipses in Figure 4. In the case of a filled cavity, two additional pores are resolved (indicated by yellow ellipses) corresponding to the area between the hexagon and the phenyl ring of the inner molecule.

Spinning in a Chiral Bearing. It is noteworthy that except for the densely packed linear pattern **DP** of the C_{2v}-symmetric **3,3′-BTP** molecules, the unit cell symmetries of all the other 2D structures are C_s-symmetric, and therefore, all monolayer structures resemble enantiomeric, homochiral domains at the 2D solid|liquid or solid|gas interface (see, e.g., Figures 1 and 3). Note the absence of prochirality in the **3,3′-BTP** molecule which is a common reason for the observation of enantiomorphic domains at interfaces because of the formation of two nonidentical yet plane symmetric adsorbed species. As the molecules are truely achiral, the supramolecular chirality is entailed solely by the asymmetric 2D H-bonding network. This chirality is especially intriguing for the hexagonal structure as it offers chiral pores which might be exploited as recognition patterns for the enantioselective adsorption of chiral molecules.

STM constant current image sequences at the solid|liquid interface, recorded with a scan speed of 10 μm·s^{-1} corresponding to an image frequency of 0.1 Hz, clearly show rotating bright spots in the center of the cavities (Figure 5). In this image sequence, the HBN is imaged with inverse contrast similar to the results at the solid|gas interface (Figure 5). The dark spots in Figure 3 are imaged as bright spots in Figure 5a and vice versa, and therefore, the bright spots in Figure 5a can be attributed to a bare substrate. Hence, we suggest that the circular rotation visible in the cavity center in Figure 5 can be assigned to coadsorbed oligopyridine molecules as the uniform movement of coadsorbed solvent molecules would result in a homogeneous contrast in the cavity.[32]

Furthermore, the rotating bright spots are located in discrete orientations in the cavitiy. In the STM images, six possible orientations of the coadsorbed **3,3′-BTP** molecules in the center of the hexagon can be observed, which is in agreement with the 6-fold symmetry of the cavity. The image sequence and the tentative models in Figure 5 exemplarily show four of the six possible adsorption geometries of the coadsorbed oligopyridine molecules highlighted in a particular HBN cavity. The remaining two orientations can be found in neighboring cavities. The fact that discrete spots are found points to an overall slow rotation which is in contrast to the complementary results obtained at the solid|gas interface (see below) or other guest molecules (e.g., copper phthalocyanine) that could be imaged only as circular disks because of their high spinning frequency.[29]

A closer look at the geometric conditions in the cavity reveals that there should be a relatively strong repulsion between the center molecule and the surrounding rim of the cavity leading to a high activation barrier. Thus, we assume that the rotation follows rather a mechanism with the sequence desorption to the supernatant, (rotation), and adsorption from the supernatant. It is impossible to determine if the molecules in the sequential

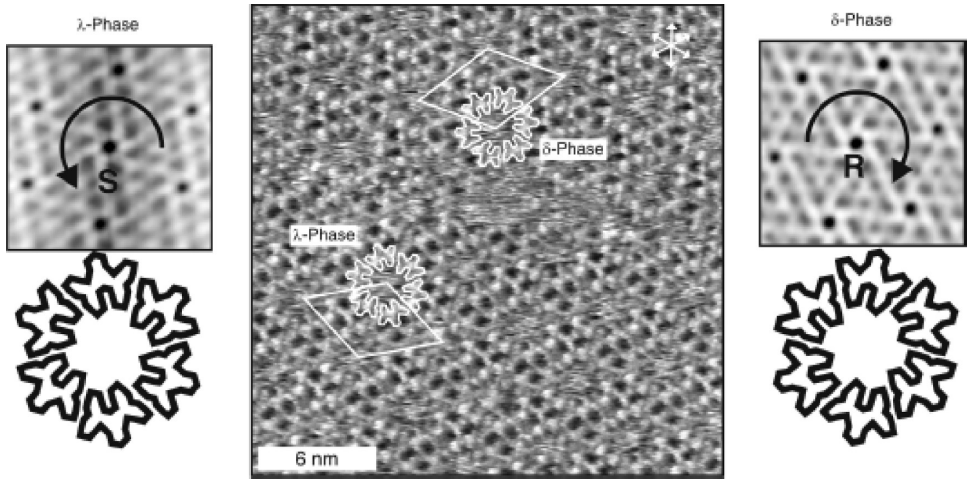

Figure 3. STM image of the hexagonal structure **Hex** at the solid|liquid interface with two enantiomorphic domains (middle). The autocorrelation images for the λ-phase (left) and the δ-phase (right) clearly reveal the homochirality of the two phases. The contour lines of the molecules highlight the position and relative arrangement of the molecules in both domains.

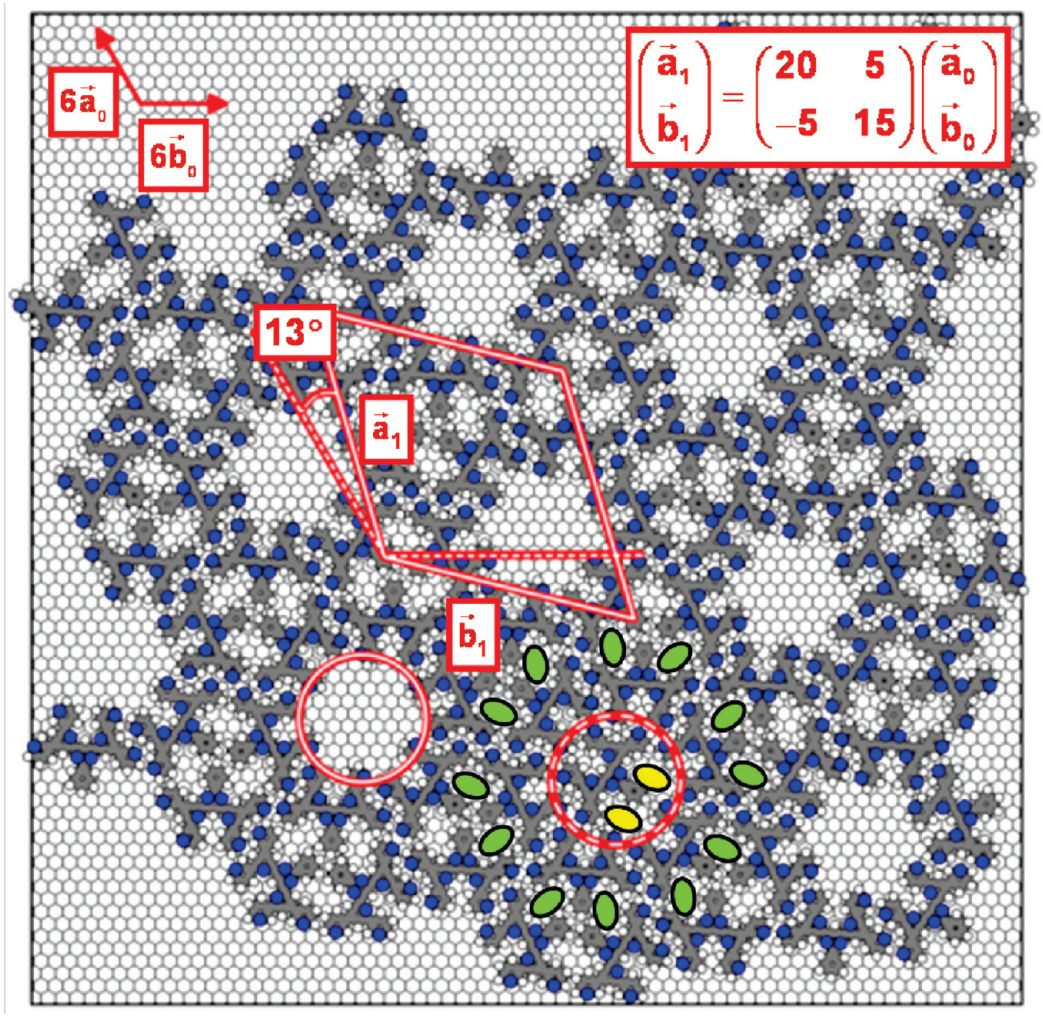

Figure 4. Commensurate model of the **Hex** network on HOPG with filled (dotted circle) and unfilled cavities (solid circle) and two different types of pores (green and yellow ellipses). The unit cell is rotated relative to the substrate vectors by 13°.

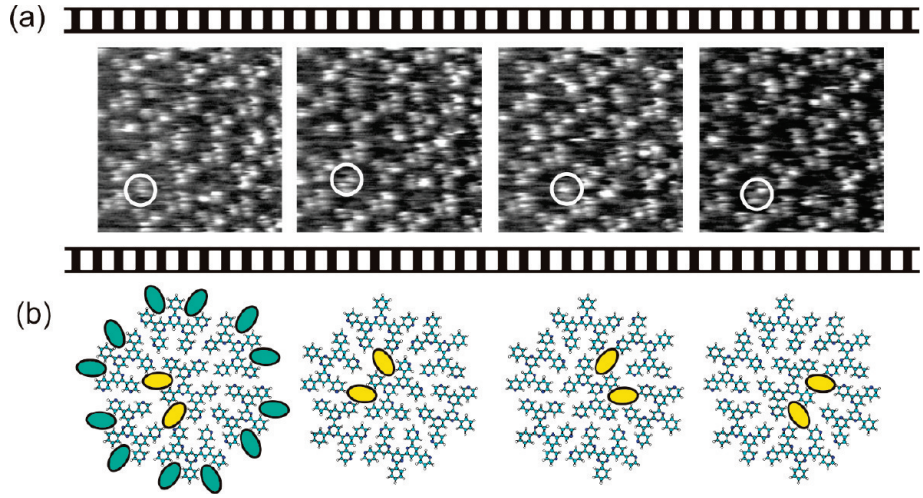

Figure 5. (a) STM image sequence of the gearwheel network **Hex** (0.1 Hz frequency) with inverse tunnelling contrast (bright: holes), showing the rotation of the **3,3′-BTP** molecule in the cavity. The asymmetric movement of the bright spots (white circle) in the cavities is due to weakly bound **3,3′-BTP** molecules. (b) Corresponding tentative molecular models for each **3,3′-BTP** configuration in the cavities with the white spots (pores) in a shown as green and yellow ellipses.

images are identical. The fact that a preferred rotational direction (unidirectional rotor) in each enantiomeric phase could not be observed is a further support for the proposed mechanism, although the HBN cavity offers a chiral surrounding (see Figure 3) similar to a ratchet with asymmetric flanks.[40]

Dependence of the Monolayer Composition on Concentration. There is no sharp concentration dependent transition between the linear and the hexagonal structures indicating a small energetic difference between the adlayer structures. At high concentrations, the linear patterns **DP** and **LinI** are

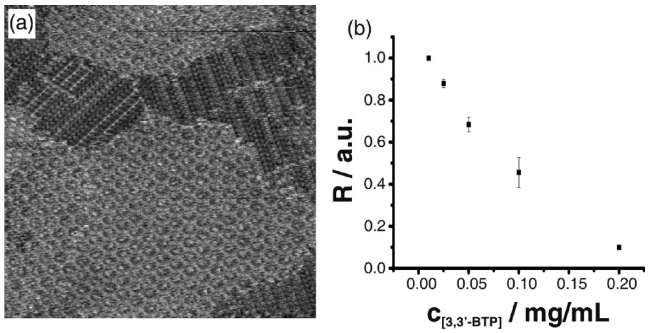

Figure 6. (a) Exemplary STM image of **3,3′-BTP** at $c = 0.05$ mg·mL^{-1} ($8 \cdot 10^{-5}$ mol·L^{-1}). The contrast between the linear and hexagonal domains is enhanced by darkening the linear and brightening the hexagonal domains in image postprocessing. (b) Plot of the surface fraction R of the gearwheel-like structure **Hex** vs the concentration of **3,3′-BTP**.

coexistent with a small amount of **Hex**. Deposited from diluted solutions, **Hex** and **LinII** dominate the monolayer structure. In contrast, a binary supramolecular system with significant energetic differences between the individual phases shows sharp phase transitions.[24]

To further analyze the influence of concentration on monolayer morphology, we plotted the fraction of the hexagonal phase R to the overall monolayer versus the concentration of the molecules in the supernatant. As the linear structures could not be differentiated from each other in the large-scale STM images, they are, therefore, subsumed to a general linear phase (**DP**, **LinI**, and **LinII**). The fraction R of the hexagonal phase versus the concentration of the applied solution shows a decrease of the surface coverage with increasing concentration (Figure 6). In the investigated concentration range, mainly limited by the solubility of the oligopyridine and the minimal amount of solute necessary to form a stable monolayer, the fraction of the hexagonal pattern never becomes zero. This indicates that the energetic differences between the adlayer structures are marginal. More coexistence images of the monolayer at different concentrations are shown in Supporting Information, Figure S1.

Solid|Gas Interface. As shown above, the structures at the liquid|solid interface are strongly governed by the presence of the solvent molecules, i.e., the concentration in the supernatant solution. To verify how far the adlayer structures themselves and their dynamic properties depend on the presence of the solution, we have formed similar adlayers by vapor deposition of **3,3′-BTP** onto HOPG in UHV.

Hexagonal Structure. At the solid|gas interface, only two different assemblies could be found, a hexagonal and a linear one. Figure 7 shows an exemplary STM image of the hexagonal **Hex** structure which shows the features corresponding to the pattern of **Hex** found at the solid|liquid interface (Figure 1d). Usual domain sizes are larger than 100×100 nm^2. The superimposed molecular outlines in b reveal the orientation and position of the molecules in the structure. As in the case for the solid|liquid interface, the inner cavity of the hexagon provides enough adsorption space for a single **3,3′-BTP** molecule. Randomly distributed filled and unfilled cavities indicated by dashed and solid circles can be distinguished in the images (Figure 7). This is coincident with the results obtained at the solid|liquid interface, where the cavities are filled with additional oligopyridine molecules (see above) and not with solvent molecules. Also visible are the pores (green and yellow ellipses) in the monolayer as described above.

The **Hex** structure obtained at the solid|gas interface qualitatively and quantitatively agrees with the hexagonal structure observed at the solid|liquid interface. In particular, the vectors of the hexagonal unit cell have lengths of $a_1 = b_1 = 4.44 \pm 0.05$ nm, and the molecular arrangement as visible in Figure 7b is identical to the model in Figure 4. Subsequent imaging of a **Hex** region using a 2 orders of magnitude higher tunnelling current revealed atomic resolution of the HOPG substrate. A comparison of the subsequent images showed that the **Hex** unit cell vectors are rotated by $13.9 \pm 1°$ with respect to the HOPG lattice vectors, again in agreement with the findings for the solid|liquid interface. Hence, the formation of the **Hex** phase is independent of the presence or absence of solvent molecules, which emphasizes the point that the main properties and characteristics of the structure can be understood without taking solvent molecules into account.

The submolecularly resolved STM image of the **Hex** network (Figure 7b) reveals two different types of occupied cavities. Cavities with fixed molecules can be easily distinguished from cavities with a rather blurred representation indicating vibrations and/or (frustrated) rotation of the guest molecules. The desorption barrier at the solid|gas interface is expected to be higher compared to the solid|liquid interface because of the absence of a competing solvation of the adsorbates. These findings support the proposed adsorption|desorption or hopping mechanism for the guest molecule rotation at the solid|liquid interface. As in this model, a higher desorption barrier results in a slower rotation frequency. Indeed, static molecules could only be observed at the solid|gas interface. Image series of the same area over several minutes at the solid|gas and solid|liquid interface unambigously show the difference in mobility between the two interfaces (see Supporting Information, Figure S2).

In a previous study, Breitruck et al. showed that a network similar to the **Hex** network could be observed at the graphite|vacuum interface by adding single Cu atoms to a quadratic adlayer of the isomeric **2,4′-BTP** molecules on HOPG.[41] This results in a porous structure with a hexagonal unit cell of $a_1 = b_1 = 4.61 \pm 0.05$ nm. Contrary to the present network held together by hydrogen bonding interactions, the main intermolecular forces in the metal organic network are based on metal ligand interactions. In this case, the enlarged molecule molecule distances result in an enlarged unit cell which in turn entails a larger cavity diameter. Therefore, excess **2,4′-BTP** molecules coadsorbed into the cavities have enough space for unhindered rotational motion. Rotation with a frequency higher than the scan frequency resulted in a disk shaped appearance of the spinning molecules.[29,41−43]

Linear Structure. After depositing excess molecules on the graphite surface and using a lower desorption temperature (546 K) than that for the preparation of the hexagonal network (551 K), a densely packed linear structure was formed. Figure 8a shows an exemplary STM image of this densely packed network which corresponds to **DP** found at the solid|liquid interface at high concentration (see above and Figure 1).[9] The unit cell parameters were determined to $a_1 = 2.62 \pm 0.05$ nm and $b_1 = 1.7 \pm 0.03$ nm, enclosing an angle of $90 \pm 1°$.

Figure 8b shows a proposed structure model with a rectangular unit cell for **DP** with $a = 2.70$ nm and $b = 1.70$ nm including an angle of $90 \pm 1°$. Vector b is commensurate to the underlying substrate, and vector a has a commensurability of higher order. The resulting packing density is 0.436 molecules·nm^{-2}. Both patterns **Hex** and **DP** coexist at the interface which we attribute to the similarity of the packing densities. The angle of $30 \pm 1°$ between **DP** and the underlying substrate was determined from images showing **Hex** and **DP** in coexistence (see Supporting Information, Figure S3).

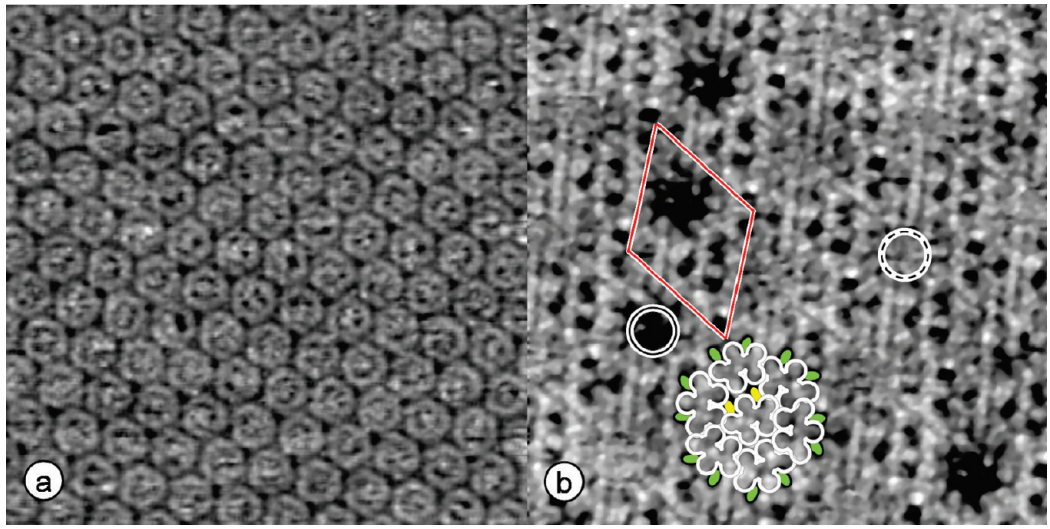

Figure 7. (a) Hexagonal network (**Hex**) formed by **3,3′-BTP** molecules at the HOPG|gas interface (67 × 67 nm^2; $U_T = -1.2$ V; $I_T = 4.47$ pA). (b) Submolecularly resolved details exhibiting the chirality of the pattern with filled (dotted circle) and unfilled (solid circle) pores. The unit cell (red) is overlaid with the bright spots in its corners (see text) (17 × 17 nm^2; $U_T = -1.2$ V; $I_T = 44.7$ pA).

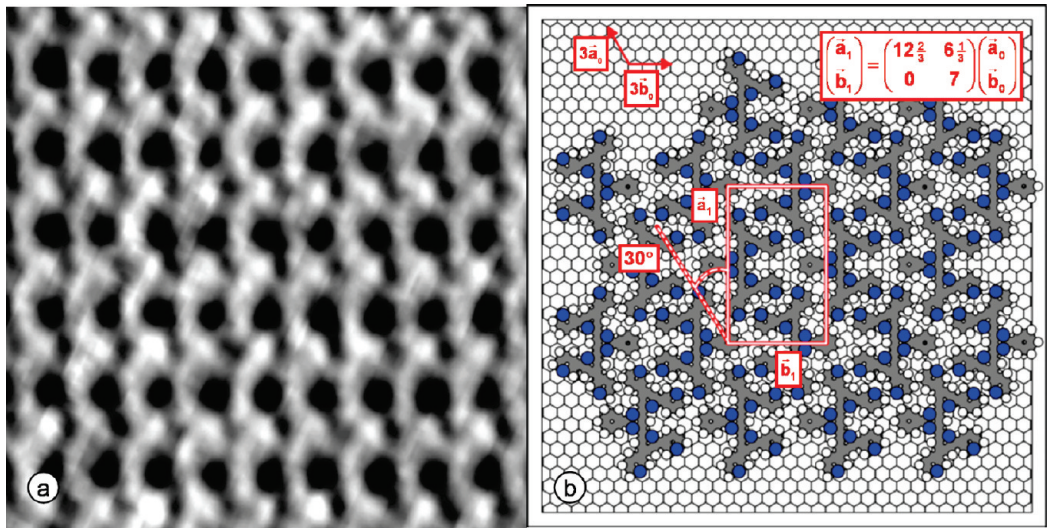

Figure 8. Dense packed structure (**DP**) formed by **3,3′-BTP** molecules on HOPG in UHV; (a) STM image (17 × 17 nm^2; $U_T = -3.75$ V; $I_T = 5.62$ pA); (b) proposed structure model.

Intermolecular Stabilization. The difference between **LinI** and **LinII** networks can be found in the intermolecular hydrogen bonding motifs. **DP** and **LinI** are stabilized through intermolecular pyridine−dimer hydrogen bonds, estimated from theoretical calculations to be −25.0 kJ·mol^{-1} and −44.4 kJ·mol^{-1}, respectively.[9]

On the contrary, the hydrogen bonding motif in **LinII** can be described with terpyridine−dimer interactions between the molecules in row direction and accompanying benzene−pyridine−dimer interactions between adjacent rows. We calculated the stabilization energy versus the CHN distance for both interactions with the Gaussian08 program package and the MP2 6-31 g(d,p) basis set. The equilibrium distance in the distance−energy potential was calculated to be 0.3 nm and the corresponding stabilization energy to be −52.2 kJ·mol^{-1}. For the estimation of the interaction energy, CHN distances derived from molecular models based on the STM images were used. Taking into account additional pyridyl−phenyl interactions with molecules in the neighbor rows (approximated with calculated *meta*-pyridyl−pyridyl interactions), the overall hydrogen bonding stabilization energy turns out to be −61.9 kJ·mol^{-1} (Supporting Information).

For the hexagonal pattern **Hex**, the intermolecular hydrogen bonding pattern can be broken down to a terpyridine−dimer interaction motif (see Supporting Information, Figures S4 and S5a). Between individual gearwheel oligomers, ortho-pyridine-dimer interactions further stabilize the oligopyridine network. The theoretical calculation of the stabilization energy versus CHN distance again yielded a Lennard−Jones-type potential with an equilibrium distance of 0.3 nm and a corresponding stabilization energy of −51.1 kJ·mol^{-1}. Taking into account additional *ortho*-pyridyl−pyridyl interactions with neighboring molecules, the overall hydrogen bonding stabilization energy comes out to be −63.6 kJ·mol^{-1}.

Semiempirical calculations have shown earlier that the lateral translation of an oligopyridine molecule on an HOPG surface alters the adsorption energy only by ∼1%.[31] With these findings, we assume that the interaction energy between a single **3,3′-BTP** molecule and the substrate is independent of the adlayer structure and therefore can be considered identical in the comparison of the energies of the different structures.

Theoretical Modeling. The different adlayers found at the solid|liquid interface appear at different concentrations of **3,3′-BTP** in the supernatant. Such behavior can be governed

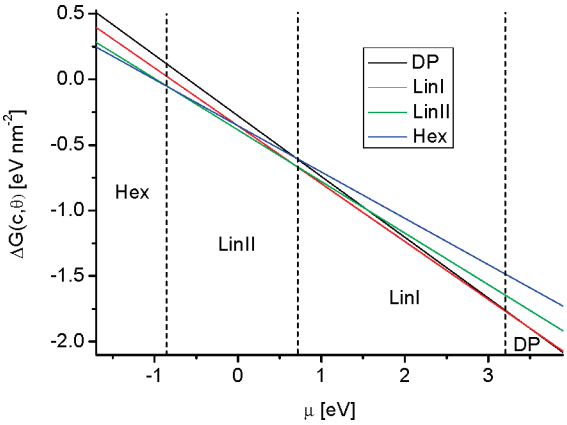

Figure 9. Semiquantitative calculation of the free enthalpy of adsorption for the different adlayer structures at the solidlliquid interface depending on the concentration in the supernatant or the chemical potential.

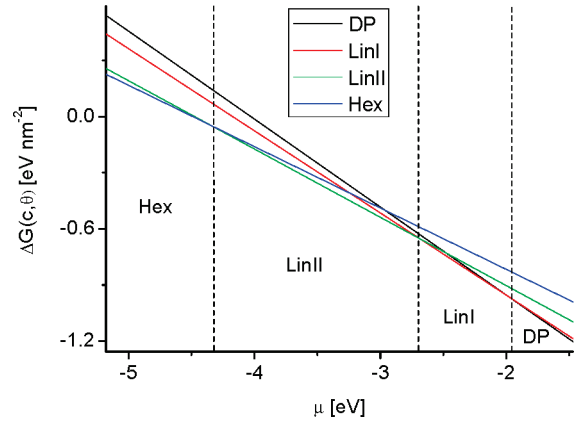

Figure 10. Free adsorption energies calculated from the COMPASS force field plotted versus the chemical potential. The phase progression is in agreement with the experimental results.

kinetically or thermodynamically. Attempts to follow the recently published thermodynamic approach remained futile, no monotonic dependence between the coverage of the linear and the coverage of the hexagonal adlayer structures according to the proposed formalism was found.[23] We attribute the inability of the appealing literature model to describe the present structural diversity to the higher complexity of our system. In order to support our assumption that the different adlayers display thermodynamically stable equilibrium structures, semiquantitative calculations were performed on the relative stability of each 2D structure. Here, on the basis of the literature, the free enthalpy of adsorption was plotted as a function of the chemical potential according to the following equation:

$$\Delta G = \rho(E_{ads} - \mu)$$

with the free energy of adsorption ΔG, the packing density ρ, the adsorption energy E_{ads} comprising the adsorbate−adsorbate and adsorbate−substrate interactions and the chemical potential of the adsorbate μ.[44−47] In equilibrium and in a given range of concentration or chemical potential, the adlayer structure with the lowest free energy should be the thermodynamically stable 2D pattern and, therefore, dominate the monolayer.

We followed two approaches. In the first set of calculations, the adsorption energy was composed of the free adsorption enthalpy for **3,3′-BTP** and the estimated intermolecular interactions based on hydrogen bonding (see above). In the present approximation, the experimentally derived adsorption enthalpy from our previous work[29] is used and regarded as independent from the adlayer structure. For the covered surface area per molecule, the experimental values from the STM results were taken. Figure 9 qualitatively displays in straight lines the most stable adlayer depending on the chemical potential or concentration in the supernatant. Two results have to be mentioned: (i) Each 2D structure shows a distinct concentration range in which stability is expected; (ii) in agreement with the experimental results, the order of appearance of the different structures is **DP**, **LinI**, **LinII**, and **Hex** with monotonically decreasing concentration or chemical potential.

In a second set of calculations, the free adsorption enthalpies as a function of the chemical potential were calculated from adsorption enthalpies obtained from force field calculations at the solidlgas interface. Although the influence of the solvent on the formation of the 2D patterns by the restriction to the solidlgas interface is neglected, the corresponding experimental results between the solidlliquid and the solidlgas interface (see above) clearly prove that such a simplification in the calculations is justified. We used the common COMPASS, Dreiding, UFF, and CVFF force fields to model the thermodynamic behavior of the comparatively large oligopyridine molecules at interfaces. Independent of the used force field, the calculations without any experimental data input did not result in similar phase orders as observed experimentally. Note, however, that the correct prediction of the stability order requires the accurate description of the subtle balance between molecule−substrate and molecule−molecule interactions which the used force fields are obviously not designed for. After using commensurate unit cells with parameters similar to the experimentally derived parameters, the adsorption energies calculated with the COMPASS force field render all four structures stable in the same order as that derived from the experiment (Figure 10). The adsorbed molecules in the calculated monolayers, however, do not adopt a coplanar configuration (Supporting Information, Figure S10). In fact, the terminal pyridyl rings are slightly rotated out of plane, therefore weakening the adsorbate−substrate interaction and resulting in a rise in the adsorption energy.

Experimentally, phase coexistence was observed throughout the investigated concentration range. In the theoretical model, the relative stability of the 2D structures and therefore their ratio in the monolayer is given by the difference in the free adsorption enthalpies $\Delta\Delta G$. At the intersection of the straight lines, $\Delta\Delta G$ equals zero, and the adlayer structures are predicted to be coexistent at the given chemical potential. Furthermore, the very similar slopes predict a rather broad concentration range around the intercept where two or more phases have a very low $\Delta\Delta G$ and, therefore, a similar thermodynamic stability. This agrees well with the experimentally observed phase coexistence. In addition, the chemical potential range in which **LinII** is the most stable phase is much broader and for **LinI** much narrower than that found in the semiquantitative calculation (Figure 9). This is in good agreement with the observation that at low concentrations only the **LinII** phase was found in coexistence with the **Hex** phase. However, the applied model has its limitations. It does not describe the high stability of the **Hex** phase throughout the investigated concentration range. For the theoretical results presented so far, we did not consider the coadsorption of a seventh oligopyridine molecule into the cavity. When calculating the free enthalphy of adsorption considering a seven molecule unit cell, **Hex** becomes thermodynamically most stable in the middle concentration range with **LinII** stable at lower chemical

potentials. This indicates, that (i) the coadsorption plays a significant role in the stabilization of the oligopyridine monolayer and that (ii) as a seventh molecule can only be incorporated after formation of the cavity the influence of rather complex kinetic effects on monolayer formation and stability shall not be neglected. The important contribution of the coadsorption to the monolayer stability is further supported by the fact that (i) after slow increase in concentration by solvent evaporation no phase transition from the **Hex** into a linear phase could be observed and that (ii) in UHV the **Hex** phase could not be formed with a low amount of occupied cavities. In addition to the purely thermodynamic considerations, the calculations permit one to derive a more precise adsorbate−substrate relationship based on the most stable and/or the most probable configuration. As revealed by DFT calculations, an individual molecule adopts an orientation with its C_2 axis perpendicular to a primitive substrate lattice vector, continuing the AB graphene layer structure (Supporting Information, Figure S8). In the **Hex** structure calculated with UFF, the C_2 axis is rotated 81.5° with respect to the substrate lattice vector (Supporting Information, Figure S9). In the experiment, we found an angle of 85 ± 1°. In addition, the differences in stabilization energies for a given force field are rather small, whereas the differences in stabilization energies between the used force fields are comparatively large. Therefore, we conclude that the subtle differences between the experimentally found adlayer structures are not sufficiently described by the used force fields. Our results are of eminent significance as this contribution is one of the first attempts where force field calculations of periodic monolayers built up from rather large organic molecules on surfaces are used to describe the thermodynamic monolayer stability. However, to accurately describe and predict the thermodynamic behavior of complex systems customized and refined force fields are needed.

Conclusions

In the present contribution, we could demonstrate the rich phase behavior of an oligopyridine at the HOPG|liquid and HOPG|gas interface. The dominating phase can be controlled by the concentration of the supernatant and the surface coverage or the temperature of preparation, respectively. The order of appearance of the different adlayer structures follows the order of packing density, which could be proven by semiquantitative calculations. More profound calculations support the experimental results by thermodynamic considerations and furthermore allow one to derive a more precise model for the adsorbate−substrate relationship for the different phases.

The most intriguing phase is a hexagonal structure comprising two types of constituting units, the hexagon forming molecules and an oligopyridine guest molecule within the central cavity. The guest molecule is able to show an apparent rotation within the cavity. From the chirality of the cavities, it is expected that the rotation displays a preferred direction as a unidirectional motor. Still, at room temperature at the solid|liquid interface only a statistical rotation can be observed, which is attributed to a desorption−readsorption mechanism supported by comparison with the results at the solid|gas interface. The rich phase behavior and the host−guest capabilities demonstrate that a concentration dependent structural diversity is a feasible approach for fine-tuning the properties of molecular monolayers. Ongoing experiments are directed toward a further control of the subtle interplay between the guest-rim and adsorbate−substrate interactions by variation of the surrounding conditions and fine-tuning of the molecular structure.

Acknowledgment. This work was financially supported by the *Deutsche Forschungsgemeinschaft* DFG within the Collaborative Research Centre (*Sonderforschungsbereich*) SFB 569.

Supporting Information Available: Concentration dependent and coexistence STM images; hydrogen bonding network of **Hex**; and calculation results. This material is available free of charge via the Internet at http://pubs.acs.org.

References and Notes

(1) Berner, S.; de Wild, M.; Ramoino, L.; Ivan, S.; Baratoff, A.; Güntherodt, H. J.; Suzuki, H.; Schlettwein, D.; Jung, T. A. *Phys. Rev. B* **2003**, *68*, 115410.

(2) Roos, M.; Hoster, H. E.; Breitruck, A.; Behm, R. J. *Phys. Chem. Chem. Phys.* **2007**, *9*, 5672–5679.

(3) Barrena, E.; de Oteyza, D. G.; Dosch, H.; Wakayama, Y. *ChemPhysChem* **2007**, *8*, 1915–1918.

(4) Vidal, F.; Delvigne, E.; Stepanow, S.; Lin, N.; Barth, J. V.; Kern, K. *J. Am. Chem. Soc.* **2005**, *127*, 10101–10106.

(5) Stöhr, M.; Wahl, M.; Galka, C. H.; Riehm, T.; Jung, T. A.; Gade, L. H. *Angew. Chem.* **2005**, *117*, 7560−7564; *Angew. Chem., Int. Ed.* **2005**, *44*, 7394−7398.

(6) Ruben, M.; Payer, D.; Landa, A.; Comisso, A.; Gattinoni, C.; Lin, N.; Collin, J.-P.; Sauvage, J.-P.; De Vita, A.; Kern, K. *J. Am. Chem. Soc.* **2006**, *128*, 15644–15651.

(7) Schull, G.; Douillard, L.; Fiorini-Debuisschert, C.; Charra, F.; Mathevet, F.; Kreher, D.; Attias, A. J. *Nano Lett.* **2006**, *6*, 1360–1363.

(8) Cyr, D. M.; Venkataraman, B.; Flynn, G. W. *Chem. Mater.* **1996**, *8*, 1600–1615.

(9) Meier, C.; Ziener, U.; Landfester, K.; Weihrich, P. *J. Phys. Chem. B* **2005**, *109*, 21015–21027.

(10) Mamdouh, W.; Uji-i, H.; Ladislaw, J. S.; Dulcey, A. E.; Percec, V.; De Schryver, F. C.; De Feyter, S. *J. Am. Chem. Soc.* **2006**, *128*, 317–325.

(11) Pineider, F.; Mannini, M.; Sessoli, R.; Caneschi, A.; Barreca, D.; Armelao, L.; Cornia, A.; Tondello, E.; Gatteschi, D. *Langmuir* **2007**, *23*, 11836–11843.

(12) Herwig, K. W.; Matthies, B.; Taub, H. *Phys. Rev. Lett.* **1995**, *75*, 3154.

(13) Li, C.-J.; Zeng, Q.-D.; Wang, C.; Wan, L.-J.; Xu, S.-L.; Wang, C.-R.; Bai, C.-L. *J. Phys. Chem. B* **2003**, *107*, 747–750.

(14) Lackinger, M.; Griessl, S.; Heckl, W. M.; Hietschold, M.; Flynn, G. W. *Langmuir* **2005**, *21*, 4984–4988.

(15) Kampschulte, L.; Lackinger, M.; Maier, A.-K.; Kishore, R. S. K.; Griessl, S.; Schmittel, M.; Heckl, W. M. *J. Phys. Chem. B* **2006**, *110*, 10829–10836.

(16) Mourran, A.; Ziener, U.; Möller, M.; Suarez, M.; Lehn, J.-M. *Langmuir* **2006**, *22*, 7579–7586.

(17) Mamdouh, W.; Uji-i, H.; Dulcey, A. E.; Percec, V.; De Feyter, S.; De Schryver, F. C. *Langmuir* **2004**, *20*, 7678–7685.

(18) Vanoppen, P.; Grim, P. C. M.; Rücker, M.; De Feyter, S.; Moessner, G.; Valiyaveettil, S.; Müllen, K.; De Schryver, F. C. *J. Phys. Chem.* **1996**, *100*, 19636–19641.

(19) De Feyter, S.; Grim, P. C. M.; Rücker, M.; Vanoppen, P.; Meiners, C.; Sieffert, M.; Valiyaveettil, S.; Müllen, K.; De Schryver, F. C. *Angew. Chem.* **1998**, *110*, 1281−1284; *Angew. Chem., Int. Ed.* **1998**, *37*, 1223−1226.

(20) Lei, S. B.; Wang, C.; Yin, S. X.; Bai, C. L. *J. Phys. Chem. B* **2001**, *105*, 12272–12277.

(21) Lei, S. B.; Yin, S. X.; Wang, C.; Wan, L. J.; Bai, C. L. *Chem. Mater.* **2002**, *14*, 2837–2838.

(22) Shao, X.; Luo, X.; Hu, X.; Wu, K. *J. Phys. Chem. B* **2006**, *110*, 1288–1293.

(23) Lei, S.; Tahara, K.; De Schryver, F. C.; Van der Auweraer, M.; Tobe, Y.; De Feyter, S. *Angew. Chem.* **2008**, *120*, 3006−3010; *Angew. Chem.* **2008**, *47*, 2964−2968.

(24) Kampschulte, L.; Werblowsky, T. L.; Kishore, R. S. K.; Schmittel, M.; Heckl, W. M.; Lackinger, M. *J. Am. Chem. Soc.* **2008**, *130*, 8502–8507.

(25) Zhang, X.; Chen, Q.; Deng, G.-J.; Fan, Q.-H.; Wan, L.-J. *J. Phys. Chem. C* **2009**, *113*, 16193–16198.

(26) Zhang, X.; Chen, T.; Chen, Q.; Deng, G.-J.; Fan, Q.-H.; Wan, L.-J. *Chem.−Eur. J.* **2009**, *15*, 9669–9673.

(27) Foster, J. S.; Frommer, J. E. *Nature* **1988**, *333*, 542–545.

(28) Tait, S. L. *ACS Nano* **2008**, *2*, 617–621.

(29) Meier, C.; Landfester, K.; Künzel, D.; Markert, T.; Gross, A.; Ziener, U. *Angew. Chem.* **2008**, *120*, 3881−3885; *Angew. Chem.* **2008**, *47*, 3821−3825.

(30) Ziener, U. *J. Phys. Chem. B* **2008**, *112*, 14698–14717.

(31) Meier, C.; Landfester, K.; Ziener, U. *J. Phys. Chem. C* **2009**, *113*, 1507–1514.
(32) Tahara, K.; Furukawa, S.; Uji-i, H.; Uchino, T.; Ichikawa, T.; Zhang, J.; Mamdouh, W.; Sonoda, M.; De Schryver, F. C.; De Feyter, S.; Tobe, Y. *J. Am. Chem. Soc.* **2006**, *128*, 16613–16625.
(33) Li, Z.; Han, B.; Wan, L. J.; Wandlowski, T. *Langmuir* **2005**, *21*, 6915–6928.
(34) Ye, Y.; Sun, W.; Wang, Y.; Shao, X.; Xu, X.; Cheng, F.; Li, J.; Wu, K. *J. Phys. Chem. C* **2007**, *111*, 10138–10141.
(35) Griessl, S. J. H.; Lackinger, M.; Jamitzky, F.; Markert, T.; Hietschold, M.; Heckl, W. M. *J. Phys. Chem. B* **2004**, *108*, 11556–11560.
(36) Griessl, S. J. H.; Lackinger, M.; Jamitzky, F.; Markert, T.; Hietschold, M.; Heckl, W. M. *Langmuir* **2004**, *20*, 9403–9407.
(37) MacLeod, J. M.; Ivasenko, O.; Perepichka, D. F.; Rosei, F. *Nanotechnology* **2007**, *18*, 424031.
(38) Ivasenko, O.; MacLeod, J. M.; Chernichenko, K. Y.; Balenkova, E. S.; Shpanchenko, R. V.; Nenajdenko, V. G.; Rosei, F.; Perepichka, D. F. *Chem. Commun.* **2009**, 1192–1194.
(39) Griessl, S.; Lackinger, M.; Edelwirth, M.; Hietschold, M.; Heckl, W. M. *Single Mol.* **2002**, *3*, 25–31.
(40) Chiaravallotti, F.; Gross, L.; Rieder, K.-H.; Stojkovic, S. M.; Gourdon, A.; Joachim, C.; Moresco, F. *Nature Mater.* **2007**, *6*, 30–33.
(41) Breitruck, A.; Hoster, H. E.; Meier, C.; Ziener, U.; Behm, R. J. *Surf. Sci.* **2007**, *601*, 4200–4205.
(42) Gimzewski, J. K.; Joachim, C.; Schlittler, R. R.; Langlais, V.; Tang, H.; Johannsen, I. *Science* **1998**, *281*, 531–533.
(43) Wintjes, N.; Bonifazi, D.; Cheng, F.; Kiebele, A.; Stöhr, M.; Jung, T.; Spillmann, H.; Diederich, F. *Angew. Chem.* **2007**, *119*, 4167−4170; *Angew. Chem., Int. Ed.* **2007**, *46*, 4089−4092.
(44) Gross, A. *J. Comput. Theor. Nanosci.* **2008**, *5*, 894–922.
(45) Reuter, K.; Scheffler, M. *Phys. Rev. B* **2001**, *65*, 035406.
(46) Kucera, J.; Gross, A. *Langmuir* **2008**, *24*, 13985–13992.
(47) Künzel, D.; Markert, T.; Gross, A.; Benoit, D. M. *Phys. Chem. Chem. Phys.* **2009**, *11*, 8867–8878.

JP910029Z